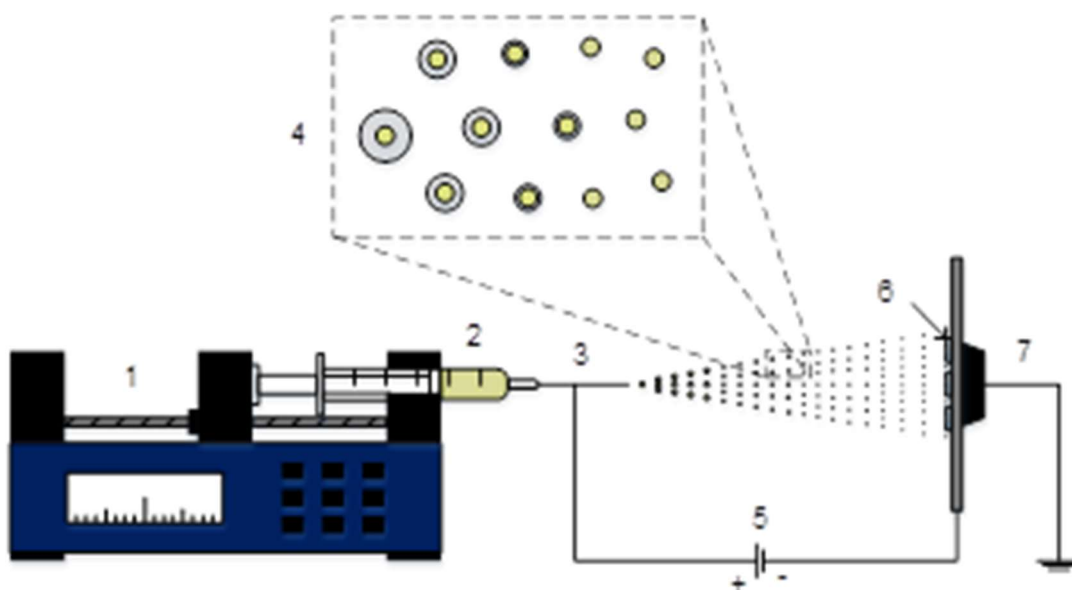


Antimicrobial surfaces with self-cleaning properties functionalized by photocatalytic ZnO electro sprayed coatings

Please, cite as follows:

Laura Valenzuela, Ana Iglesias, Marisol Faraldos, Ana Bahamonde, Roberto Rosal, Antimicrobial surfaces with self-cleaning properties functionalized by photocatalytic ZnO electro sprayed coatings, *Journal of Hazardous Materials*, Volume 369, 2019, Pages 665-673, ISSN 0304-3894, <https://doi.org/10.1016/j.jhazmat.2019.02.073>.



Antimicrobial surfaces with self-cleaning properties functionalized by photocatalytic ZnO electro sprayed coatings

Laura Valenzuela^{1,2}, Ana Iglesias^{2,*}, Marisol Faraldos^{2,*}, Ana Bahamonde², Roberto Rosal^{1,*}

¹ Department of Chemical Engineering, University of Alcalá, E-28871 Alcalá de Henares, Madrid, Spain

² Instituto de Catálisis y Petroleoquímica, ICP-CSIC, Marie Curie 2, 28049 Madrid, Spain

Corresponding authors: ana.iglesias@icp.csic.es, mfaraldos@icp.csic.es, roberto.rosal@uah.es

Abstract

Photoactive coatings of sol-gel ZnO suspensions were electro sprayed on glass substrates to produce self-cleaning antimicrobial functionalized surfaces. ZnO-functionalized materials exhibited a uniform external surface consisting of a pattern of microspheres with diameters in the 100–300 nm range. Electro spray allowed surface densities up to 0.30 mg cm⁻² that displayed considerable hydrophilicity. Water contact angle decreased with UV irradiation to values below 10°. Two different UV doses were tested by adjusting the irradiation time to simulate Summer-Spring and Winter-Fall conditions. The functionalized coatings showed excellent photocatalytic properties towards the photodegradation of Methylene blue. The electro sprayed surfaces also displayed antibacterial activity against *Staphylococcus aureus*, with >99.5% reduction in the number of culturable cells. The biocidal activity is attributed to the photogenerated reactive oxygen species on the surface of ZnO coatings and the bioavailable zinc ions produced from ZnO dissolution. The photoactive coatings kept surfaces free from bacterial colonization and biofilm formation.

Keywords: Photocatalysis; Zinc oxide; Electro spray; Self-cleaning; Antimicrobial surfaces

1. Introduction

In the last decades, increased resistance to conventional antibiotics has led to important research in the development of alternative strategies for preventing pathogen dissemination. Antimicrobial surfaces containing a biocidal agent inhibit or reduce microbial growth capacity on the surface of materials [1]. In addition to this microbial proliferation inhibition, antimicrobial coatings may also confer additional properties, such as greater surface uniformity, higher physical-chemical resistance, as well as self-cleaning properties, with the great advantage of reducing cleaning hours and costs [2]. Several semiconductor oxides exhibit antimicrobial activity due to light-catalyzed chemical reactions that don't involve the release of any harmful compounds. Photocatalytic antimicrobial coatings containing metal oxide nanoparticles have shown great potential for inactivating a wide range of microorganisms and organic pollutants for a variety of applications ranging from building materials to textile applications [3-5].

Among photocatalytic materials, ZnO attracts considerable technological interest due to its large variety of forms including complex hierarchical micro/nanoarchitectures with enhanced chemical and photoelectronic properties [6,7]. ZnO is characterized by a direct wide band-gap similar to anatase TiO₂ (3.4 eV), appropriate location of conduction and valence bands, high oxidation capacity, low cost, abundance and a large exciton binding

energy at room temperature (60 meV) [8]. The remarkable antimicrobial activity of ZnO can be attributed to: (i) formation of reactive oxygen species (ROS) [9-13], (ii) release of zinc ions [14-17], (iii) electrostatic interactions resulting in cell membrane damage [18-20], and (iv) nanoparticle internalization [13,18,21]. The relative importance of these mechanisms depends on the medium and the physicochemical properties of zinc oxide nanoparticles [17].

Electro spray is a low-cost scalable technique to transform fine and monodisperse droplets into solid particles that can create thin uniform coatings [22]. Electrostatic deposition methods are advantageous over conventional techniques, since they allow preparing nanostructured coatings on multiple substrates with precise control of the deposited material amount [23,24]. By applying a high voltage, positively charged drops are generated from the tip of a liquid jet and driven towards a grounded collector. As solvent evaporates, charge density approaches Rayleigh limit and electrostatic repulsion overcomes surface tension so that the primary droplets undergo Coulomb fission into smaller droplets [25]. The solid particles become deposited on the grounded collector eventually forming tightly packed layers [26].

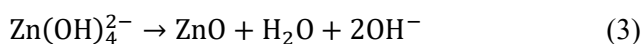
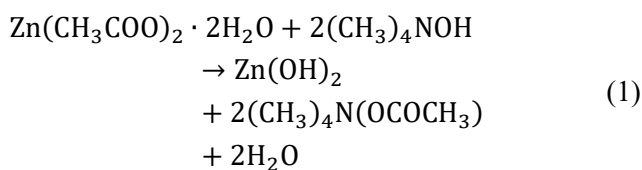
In this work, we studied the self-cleaning and antimicrobial activity of photoactive coatings prepared from ZnO suspensions electro sprayed on glass substrates. The self-cleaning performance was assayed

using the Methylene blue-test and the antibacterial efficiency by means of cultures of the gram-positive bacterium *Staphylococcus aureus*. Different mass densities and irradiation dosages were tested. The bioactivity of coatings was studied by quantifying the number of culturable bacteria and by visualizing the formation of biofilms.

2. Materials and methods

2.1. Preparation and characterization of photocatalytic materials

Zinc oxide nanoparticles were synthesized by sol-gel method according to an improved procedure derived from Spanhel and Anderson [27]. Zinc acetate dihydrate ($\text{Zn}(\text{CH}_3\text{COO})_2 \cdot 2\text{H}_2\text{O}$), methanol (CH_3OH) and tetramethylammonium hydroxide (TMAH, $(\text{CH}_3)_4\text{NOH}$) were used as precursor, dispersing medium and base, respectively. Briefly, 0.14 M zinc acetate dihydrate was dissolved in 100 mL of methanol. After 1 h of magnetic stirring at room temperature, TMAH (25% w/w in methanol) was added dropwise until zinc acetate and TMAH reached a molar ratio 1:2. The resultant suspension was aged for 48 h to yield a stable sol, which was used for coating process without requiring any post-conditioning step. Sol-gel process involves four main stages: (i) solvation, (ii) hydrolysis, (iii) condensation and polymerization, and (iv) growth and aging [28,29]. Zinc acetate ions are solvated and stabilized in methanol. Upon addition of TMAH, zinc hydroxide, tetramethylammonium acetate and water molecules are formed (Eq. (1)). The zinc hydroxide separates into its respective ions Zn^{2+} and OH^- , followed by polymerization of the hydroxyl complex, which is finally converted to ZnO, as summarized in Eqs. (2) and (3).



Dynamic particle size and zeta potential (ζ -potential) of the ZnO nanoparticle suspensions were obtained by Dynamic Light Scattering (DLS) at 25 °C in a Zetasizer Nano ZS (Malvern). The pH and the electrical conductivity were recorded using a multimeter (MM 40+, Crison). Surface tension was measured through the pendant drop technique by a Drop Shape Analyzer (DSA25, Krüss) using ImageJ software for image processing [30]. Band-gap was determined as of the UV-vis diffuse reflectance spectra obtained using an Agilent Cary 5000 equipment. The crystal structure of

the nanoparticle powders was characterized by X-ray Diffraction (PANalytical X'Pert Pro). Crystallite size was estimated by means of Scherrer's equation.

2.2. Fabrication and characterization of electrospayed surfaces

The electrospaying of ZnO nanoparticle suspension was carried out in the device schematically shown in Fig. 1. Briefly, the ZnO sol prepared as above indicated, was pumped through a stainless-steel capillary needle with 0.337 mm inner diameter. A high voltage of 20 kV (Heinzinger LNC 30000) was applied between the needle and a grounded collector separated 15 cm. A syringe pump (PHD22/2000, Harvard) provided a constant flow rate of 0.05 mL h⁻¹. The electrospay operated in a stable cone-jet mode at room temperature with 40–50% relative humidity, generating an aerosol of monodisperse charged droplets loaded with ZnO nanoparticles. Finally, the dry particles were deposited onto prewashed 13 mm diameter round glass coverslips, which were attached to the collector. Two different loadings of ZnO, denoted as C(+) and C(++), were obtained by using deposition times of 150 and 300 min, respectively. Before and after electrospaying, the substrates were dried and accurately weighed.

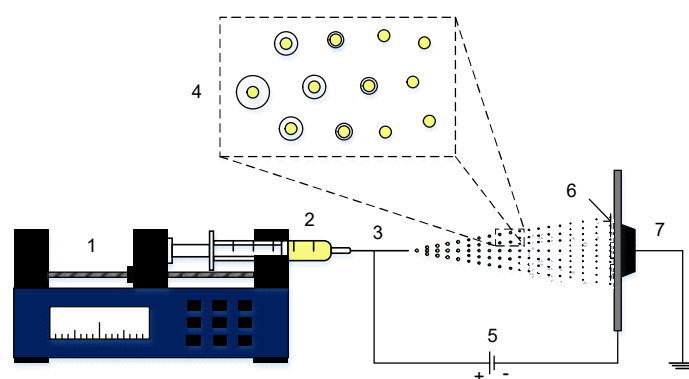


Figure 1. Scheme of the electrospay setup used for ZnO nanoparticle coating preparation. (1) Syringe pump, (2) ZnO nanoparticle suspension, (3) capillary needle, (4) aerosol formation and solvent evaporation, (5) high voltage power supply, (6) glass substrate, (7) grounded collector.

The morphology and thickness of the fabricated ZnO films were characterized by Scanning Electron Microscopy using gold-coated samples (SEM, Zeiss DSM 950). The adhesion performance of the ZnO coatings was determined by the tape test method following the ASTM D3359 standard. The wettability and hydrophobicity of the electrospayed surfaces were determined by measuring water contact angle (WCA) by the sessile drop method using a DSA25 Krüss Analyzer and three independent measurements minimum.

2.3. Self-cleaning photocatalytic behavior

The photocatalytic activity of the ZnO functionalized surfaces was evaluated by tracking the degradation of Methylene blue (MB) stain upon UV irradiation. The photodegradation tests were carried out in a closed chamber, consisting of six 15 W BBL fluorescent lamps placed 20 cm above the samples. The lamps emitted UVA light in the 306–383 nm range and the measured irradiance was $27 \pm 3 \text{ W m}^{-2}$ (broadband UV CUV-4 Kipp & Zonen radiometer). A nozzle regulated airbrush (Defynik 140, Sagola) was used to deposit 0.5 or 3.5 mL of a $5 \cdot 10^{-4} \text{ M}$ solution in acetone on ZnO coated glass coverslips. The degradation of MB stains was monitored by measuring the UV–vis Diffuse Reflectance spectra (Cary 5000, Agilent) along 10 h in the 200–800 nm interval, as the major absorption band of MB was centered at 665 nm [31,32].

2.4. Antimicrobial activity assays and bioanalytical procedures

The antibacterial activity of ZnO electrospayed surfaces was investigated using the biofilm-forming gram-positive bacteria *Staphylococcus aureus* (CECT 240). The microorganism was grown in Nutrient Broth (NB, 5 g L⁻¹ beef extract, 10 g L⁻¹ peptone, 5 g L⁻¹ NaCl, pH 7.0 ± 0.2) at 37 °C under agitation. The bioassays were conducted using two different exposure methodologies using either aerosol spraying, or liquid phase contact. As for the first, the bacteria-containing aerosol was sprayed in a sealed polypropylene chamber schematically shown in Fig. S1 (Supplementary Material, SM). A suspension of $10^8 \text{ cells mL}^{-1}$ in NB was loaded into a nebulizer, which generated an aerosol of $7 \mu\text{L cm}^{-2}$, which was applied on ZnO coated and uncoated (blank) glass coverslips. The temperature was kept at 37 °C and the relative humidity was controlled above 96% using a hygrostatic K₂SO₄ solution, according to the OIML R 121 recommendation [33]. On the second case, liquid exposure mode, functionalized and non-functionalized glass substrates were placed into sterile 24-well polystyrene plates covered with 1.8 mL cm^{-2} bacterial suspension ($10^8 \text{ cells mL}^{-1}$ in 1/500 NB). In both exposure modes, bacteria were allowed colonizing surfaces and to form biofilms for 20 h at 37 °C in dark.

Immediately after incubation, the specimens were irradiated using a UV lamp (LED BLS 13000-1, Mightex) emitting at 365 nm with an irradiance of 110.5 mW cm^{-2} (for 48 mm diameter spot). Winter-Fall, L(+), and Summer-Spring, L(++), daylight exposure conditions were simulated adjusting exposure times and spot diameter. The calculations were based on NASA Surface Meteorology and Solar Energy Database (<https://power.larc.nasa.gov/>). The average daily incident insolation reported for a horizontal surface at

the latitude of Madrid was 6.1 kW-h m^{-2} in Spring-Summer and 2.7 kW-h m^{-2} in Winter-Fall, from which 5.2% and 5.7% respectively correspond to UV irradiation. As a conservative assumption, the irradiation time of the LED lamp was adjusted to irradiate with one third of the value indicated by the solar irradiation database for Summer-Spring (2.0 kW-h m^{-2}) or Winter-Fall (1.0 kW-h m^{-2}).

Upon irradiation, the number of viable bacteria both in the liquid supernatant and adhered onto the surface was determined by plate counting following the ISO 22,196 standard. To remove non-adhered cells and recover bacteria attached to the surface SCDLP broth (Soybean casein digest broth with lecithin and polyoxyethylene sorbitan monooleate) was used. 10-fold serial dilutions were performed in sterile 96-well plates and 10 μL spots were placed on Petri dishes containing plate count agar (2.5 g L⁻¹ yeast extract, 5 g L⁻¹ tryptone, 1 g L⁻¹ glucose, 15 g L⁻¹ agar powder). Petri dishes were incubated at 37 °C for 24 h and the number of colony forming units (CFU) was determined using at least three replicates with two serial dilutions minimum.

Intracellular oxidative stress was assessed using the method of dichlorofluorescein (DCF). Briefly, 50 μL of 10 mM 2',7'-dichlorodihydrofluorescein diacetate (H₂DCFDA) stock solution were added to 150 μL of culture medium in contact with functionalized and non-functionalized surfaces in black 96-well plates. H₂DCFDA is hydrolyzed by intracellular esterases to dichlorodihydrofluorescein carboxylate anion, which is further oxidized to DCF. DCF yields a fluorescent compound in the presence of ROS [34,35]. The plates were incubated at 25 °C for 5 min and fluorescence recorded by a fluorometer (Fluoroskan Ascent FL, Thermo Scientific) every 5 min for 30 min with excitation/emission wavelengths of 485 and 528 nm, respectively.

Cell viability and membrane damage were assessed using Live/Dead BacLight Bacterial Viability Kit (Fisher Scientific). The procedure was: 10 μL of a mixture containing green-fluorescent SYTO 9 and red-fluorescent Propidium iodide (PI) stains in DMSO were added to the samples followed by 15 min incubation in darkness at room temperature. SYTO 9 stains all bacteria, whereas PI penetrates only bacteria with damaged membranes. The excitation/emission wavelengths were 488/500–575 nm for green fluorescence (SYTO 9, live cells) and 561/570–620 nm for red fluorescence (PI, dead cells).

Biofilm matrix was revealed using FilmTracer SYPRO Ruby (Fisher Scientific), a fluorochrome that labels proteins in the biofilm matrix. 200 μL of FilmTracer stain was used for every specimen followed by 30 min incubation in darkness. The biofilm was

visualized by confocal microscopy (Leica TCS-SP5) with excitation/emission at 450/610 nm. The bacteria colonizing the surfaces were visualized by Scanning Electron Microscopy (SEM, Zeiss DSM 950) after a fixation process with glutaraldehyde 5% in sodium cacodylate buffer. After 1 h of fixation at room temperature, samples were washed twice in cacodylate buffer and dehydrated with ethanol and acetone.

The soluble zinc ions released from ZnO electrospayed surfaces were quantified using Inductively Coupled Plasma Mass Spectrometry (ICP-MS, XSERIES 2, Thermo Scientific) after contact with ultrapure water at 37 °C, pH 7.2. The biological effect of soluble Zn²⁺ was assessed by measuring dose-effect responses to CFU of *S. aureus* using zinc acetate dihydrate in the 0–1000 mg Zn²⁺ L⁻¹ and bacterial cultures starting with 10⁸ cells mL⁻¹ incubated at 37 °C for 20 h. The calculation of half-maximal inhibitory concentrations (IC₅₀) was performed by fitting the experimental data to a sigmoidal curve using the Hill equation [36].

2.5. Statistical analysis

Statgraphics Centurion XVII software was used to conduct a two-way analysis of variance (ANOVA). Mean values were compared by employing Tukey's test ($p < 0.05$). Grubbs' test was performed to identify outliers, according to the ASTM E178-00 standard. Results were provided as average and standard deviation.

3. Results and discussion

3.1. Nanoparticle properties and electrospay parameters

The main properties of ZnO nanoparticle sol-gel are shown in Table 1. DLS particle size measurements showed a well-defined single peak at 171.5 ± 3.1 nm, which corresponded to the dominant size of aggregates/agglomerates in the suspension. ZnO nanoparticles in the sol-gel were negatively-charged, displaying a ζ -potential of -21.9 ± 1.6 mV at pH 7.85 ± 0.03 . The electrical conductivity (6.64 ± 0.13 mS cm⁻¹) and surface tension (33.4 ± 0.6 mN m⁻¹) of the nanoparticle suspension as produced were adequate for electrospay deposition and required no further changes. The optical properties of ZnO nanoparticles were investigated by UV-vis Diffuse Reflectance Spectroscopy and the direct band-gap was determined using Planck-Einstein relation. The calculated band-gap was 3.29 eV, in good agreement with previously reported values [29,37,38].

Droplet size in electrospay processes is known to depend on the physical properties of the suspension, mainly its electrical conductivity and surface tension, and the liquid flow rate, which also determine the emitted current [26,39]. Electrical atomization produces

monodisperse aerosols with diameters ranging from 100 μ m down to 5 nm depending on liquid properties, droplet size and suspension particle load determining the size of the dry final particles [40]. The so-called scaling laws allow estimating droplet size and emitted current of electrospay systems operating in cone-jet mode [41,42]. Scaling laws and the calculated parameters from the suspension properties are reported in Table S1, (SM). The best fits of Chen and Pui empirical data were used to determine $G(\kappa)$ and $f(\kappa)$ parameters [43]. The calculated droplet sizes were 263 and 540 nm following Fernández de la Mora and Loscertales [41], and Gañán-Calvo [42] scaling laws, respectively. According to the equations, droplet diameter and current fluctuation can be reduced by approaching feed flow rate to the minimum. The minimum values compatible with cone-jet stability were used here.

Table 1. Properties of ZnO nanoparticle suspension.

Particle size (DLS)	171.5 ± 3.1 nm
ζ -potential (pH 7.85)	-21.9 ± 1.6 mV
pH	7.85 ± 0.03
Electrical conductivity	6.64 ± 0.13 mS cm ⁻¹
Surface tension	33.4 ± 0.6 mN m ⁻¹
Band-gap	3.29 eV
Crystallite size (XRD, Scherrer)	33 nm

X-ray diffraction patterns of the ZnO xerogel and the electrospayed functionalized surface are presented in Fig. 2. The peaks are indexed as 31.61° (100), 34.25° (002), 36.09° (101), 47.38° (102), 56.45° (110), 62.72° (103), 66.19° (200), 67.77° (112), and 68.96° (201) respectively. All diffraction peaks corresponded to the characteristic hexagonal wurtzite structure of zinc oxide structure according to the ICSD files (01-079-0206). However, in the xerogel sample small additional contributions were also observed which corresponds to a residual minor phase assignable to the formation of zinc hydroxide. The relative intensity of the wurtzite diffraction peaks was similar in both samples indicating that the sol-gel electrospaying does not modify the morphology of the ZnO nanoparticles. The diffraction pattern of the ZnO electrospayed surface presented broader and lower intensity peaks caused by the low coating thickness. The crystal size of the ZnO xerogel, 33 nm, was calculated using Scherrer's equation. The significantly higher value of the DLS measurements could be attributed to the agglomeration/aggregation of primary particles, which is a dynamic process usually found in colloids that depends on the surface charge density of the particles. At pH 7.85, the surface charge of -21.9 mV corresponds to a stable suspension with moderate tendency to agglomerate.

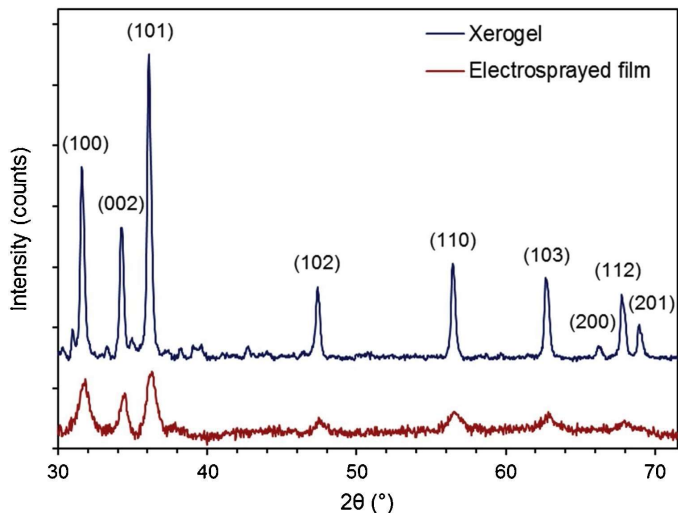


Figure 2. X-ray diffraction patterns of ZnO xerogel and ZnO electrospayed film.

3.2. Characteristics of electrospayed coatings

Fig. 3 shows SEM images including cross-sectional views and surface morphology of the ZnO-functionalized materials obtained using two different electrospay times. Top views exhibited a pattern of microspheres with diameters ranging from 100 to 300 nm. These dimensions are in good agreement with the values expected from the scaling laws for droplets that eventually form the coatings of solid particles as discussed before. The surface electrospayed for 150 min, indicated as C(+), displayed occasional gaps

between aggregates. Its thickness could be estimated from cross-sectional SEM images around $0.6 \mu\text{m}$, and the mass surface density was $0.13 \pm 0.04 \text{ mg cm}^{-2}$. The surface electrospayed for 300 min, denoted as C(++), displayed a more uniform coverage. The average thickness was $1.1 \mu\text{m}$ and the mean surface loading was $0.30 \pm 0.05 \text{ mg cm}^{-2}$. In both cases, tape test method was conducted to determine the adhesion between the film and the glass substrate, showing the highest adhesion level of 5B (ASTM D3359 standard).

The wetting properties of the ZnO electrospayed films were investigated following UV exposure simulating Winter-Fall, L(+), and Summer-Spring daylight, L(++), as indicated before. Table 2 shows WCA measurements on the surface of coated, C(+) and C(++), and uncoated, C(-), glass coverslips. The WCA on bare glass substrates was $73.1 \pm 2.0^\circ$, which did not change after UV irradiation. ZnO-functionalized non-irradiated surfaces were hydrophilic, yielding WCA of $21.1 \pm 0.9^\circ$ and $19.8 \pm 0.4^\circ$ for C(+) and C(++), respectively. Upon L(+) irradiation, the wettability increased significantly ($p < 0.5$) and surfaces turned more hydrophilic, showing WCA values around 9° .

ZnO-coated surfaces became even more hydrophilic after L(++), more intense irradiation, with WCA as low as $4.2 \pm 0.9^\circ$ and $2.8 \pm 0.4^\circ$ for low and high surface density coatings, respectively. However, the differences in WCA measurements for C(+) and C(++), coated surfaces were not significant ($p > 0.5$).

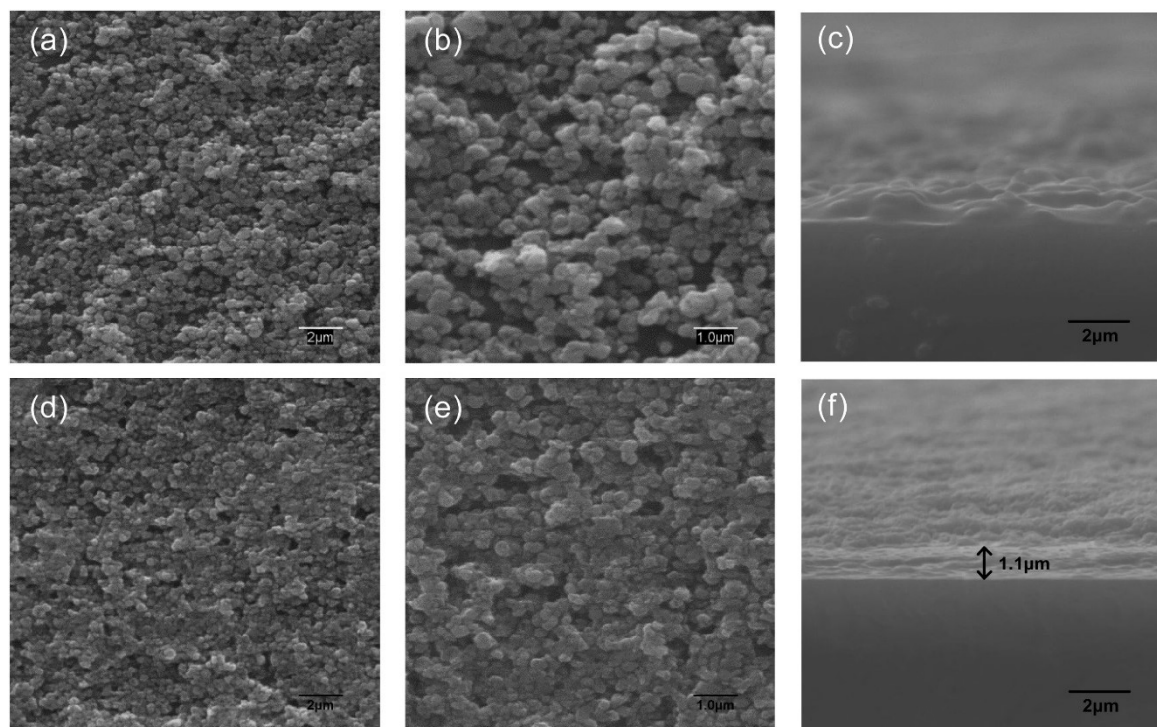


Figure 3. Top and cross-sectional SEM images of ZnO electrospayed surfaces obtained after 150 min, C(+), and 300 min, C(++): (a) and (b) top views of C(+) coating; (d) and (e) top views of C(++) coating; (c) and (f) cross-sectional views of C(+) and C(++), respectively.

Table 2. WCA (°) measurements for ZnO electro sprayed surfaces.

Substrate		Bare glass	Low surface density	High surface density
		C(-)	C(+)	C(++)
No irradiation	L(-)	73.1 ± 2.0	21.1 ± 0.9	19.8 ± 0.4
Winter irradiation	L(+)	74.2 ± 1.6	10.1 ± 1.0	8.6 ± 2.6
Summer irradiation	L(++)	73.3 ± 2.2	4.2 ± 0.9	2.8 ± 0.4

ZnO surface exhibited photo-induced hydrophilicity under UV irradiation, increasing its wettability from the initial hydrophilic character even leading to super-hydrophilicity [[44], [45], [46], [47]]. The reason is that the photogenerated electron-hole pairs on the surface react with Zn-O lattice bonds to form Zn⁺defective sites and oxygen vacancies, which interact with water molecules causing their dissociative adsorption with subsequent hydrophilicity increase [44,48,49]. This hydrophilicity increase is unstable so that the surface slowly returns to its initial state because oxygen adsorption is thermodynamically favorable over hydroxyl groups from water dissociation [44,46].

3.3. Self-cleaning photocatalytic properties

The results for the photodegradation efficiency of MB during BBL UVA irradiation are shown in Fig. 4a as a function of MB concentration and surface coating

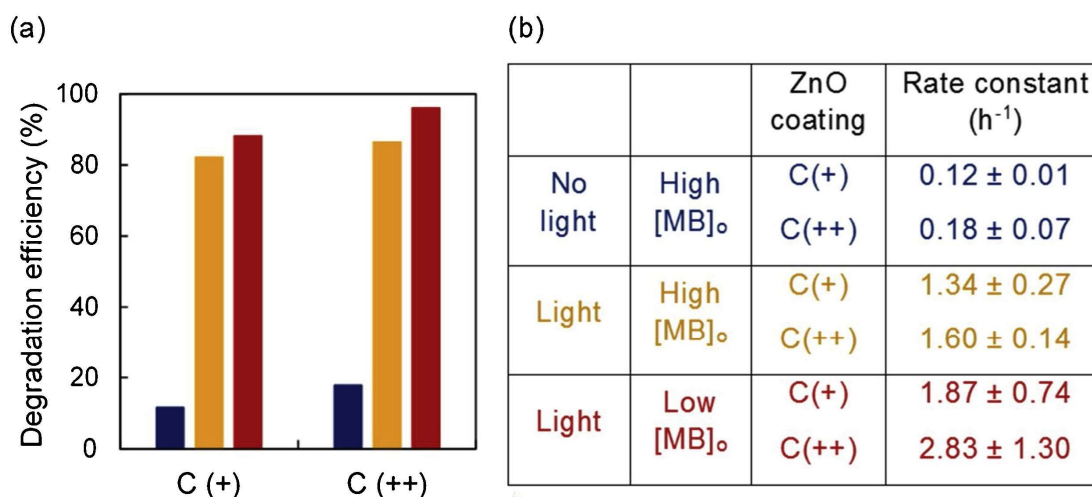


Figure 4. MB photodegradation conversions at 120 minutes (a) and pseudo-first order kinetic constants (b) in absence of irradiation (■) and under irradiation with high MB initial concentration (■) and with low MB initial concentration (■) for C(+) and C(++) ZnO coatings.

3.4. Antimicrobial activity

The antimicrobial properties of the ZnO-functionalized surfaces were assayed against *S. aureus* cells by quantifying the reduction of CFU in specimens

previously incubated for 20 h at 37 °C both in aerosol and liquid exposure modes (Fig. 5). The application of bacteria-containing aerosol either using low and high loading specimens, C(+) and C(++), respectively, or low and high irradiation, L(+) and L(++), respectively, density. Blank experiments were carried out to determine the percentage of dye degradation in the absence of photocatalyst, which was 4.9% after 120 min irradiation. Another set of runs was performed without UV irradiation on ZnO-coated specimens that showed MB removal percentages of 11.5 and 17.8% for C(+) and C(++), respectively. MB removal in dark conditions was attributed to adsorption on photocatalyst surface. Under UV irradiation, the surface of the functionalized specimens turned colorless gradually, reaching 88.2% and 96.0% degradation efficiency after 120 min using the lower MB initial concentration and for C(+) and C(++), respectively. Despite the increase in the amount of catalyst the differences between C(+) and C(++), respectively. A higher thickness led to more homogeneous coatings, which could justify the slight increase observed in the degradation efficiency. However, that improvement is not proportional to the increase of the coating density indicating that part of the deposited material is not being activated. The light penetration limits MB degradation that takes place preferably on the photocatalyst surface rather than on deeper layers of ZnO. Applying higher initial colorant concentration, the final degradation efficiency decreased to 82.2% and 86.5% for C(+) and C(++), respectively, which could be due to radiation absorption by MB [50]. Fig. 4b shows the calculated pseudo first-order kinetic constants for the photocatalytic degradation of MB on the different assayed substrates.

previously incubated for 20 h at 37 °C both in aerosol and liquid exposure modes (Fig. 5). The application of bacteria-containing aerosol either using low and high loading specimens, C(+) and C(++), respectively, or low and high irradiation, L(+) and L(++), respectively,

led to > 99.5% (> 2-log) reduction in CFU compared to C(-)L(-) controls (Fig. 5a). In specimens exposed to the liquid culture medium, a higher inhibition of bacterial growth was found (Fig. 5b–c). For cells attached to the surface of coatings C(+) and C(++) in contact with liquid culture medium, > 99.9% inhibition (3-log reduction) was reached, whereas the liquid supernatant was essentially free of viable bacteria (> 7-log reduction).

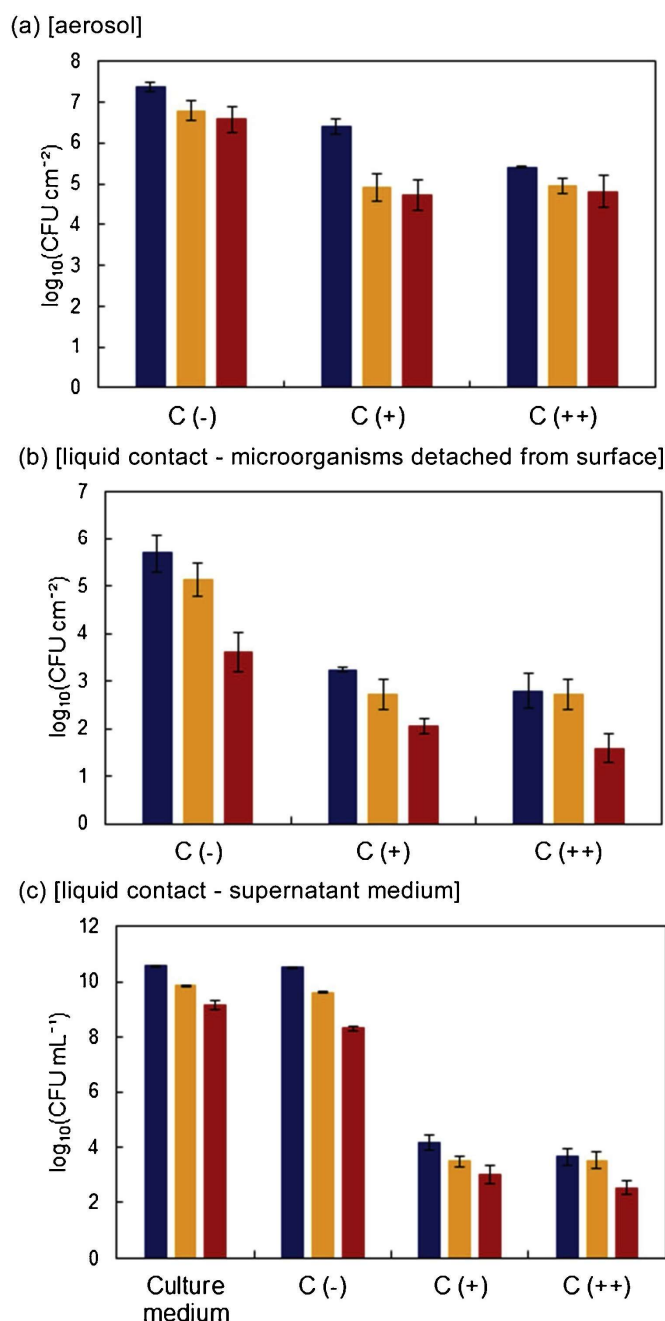


Figure 5. Colony-forming units (CFU) of *S. aureus* measured from the surface after aerosol (a) and liquid contact (b) modes, and CFU in the supernatant for the liquid exposure mode (c). Uncoated, C(-), and coated specimens with low loading, C(+), and high loading, C(++), in the absence of irradiation [L(-), ■], and upon L(+) (Winter, ■) and L(++) (Summer, ■) irradiation.

Light exposure triggers the photocatalytic activity of ZnO giving rise to ROS photogeneration on the catalyst surface [18,37, 51-53]. Photogenerated electron-hole pairs initiate a series of oxidation-reduction reactions leading to oxidizing species such as O₂^{•-}, [•]OH and H₂O₂ [38, 54-56]. ROS have been shown to penetrate cells, damaging cellular components including lipids, proteins and DNA through oxidative stress [38,57,58].

The existence of a certain antimicrobial action in the absence of irradiation suggests that the release of zinc ions from ZnO nanoparticles may take place. Zinc ions, rather than zinc oxide, were associated to cell lysis due to cell wall disruption, and damage to different cellular components upon uptake and internalization [17,52,59-61]. For that reason, the solubility of the ZnO films were studied. Fig. S2 (SM) shows the amount of zinc metal ions released into Milli-Q water per unit mass of ZnO film at 37 °C. Zinc ion concentration increased throughout the first 5 h, and reached a plateau after about 10 h with a value of ~40 mg Zn²⁺/g ZnO, which represented 6.7 mg Zn²⁺ L⁻¹ or 1.0·10⁻⁴ M for the solubilization experiment conditions. The main factors behind Zn²⁺ release from ZnO nanomaterials are morphology, particle size, surface defects, UV irradiation and the chemistry of the medium [62,63]. However, previous studies showed that ZnO nanomaterials act as zinc ions carriers, keeping Zn²⁺ concentration approximately constant in aquatic media [64]. This is due to the ZnO solubility limit, which approximately corresponds to the same 10⁻⁴ M value obtained in this work [65].

The antimicrobial effect of Zn²⁺ is shown in Fig. S3 (SM), which represents the dose-response curve for CFU inhibition in cultures containing different concentrations of Zn²⁺ cations from zinc acetate. Half-maximal inhibitory concentration (IC₅₀) of Zn²⁺ calculated through Hill equation was 0.9 ppm, somewhat lower than the previously reported value of 2.7 ppm [66]. The difference can be attributed to the different endpoints used. While Chudobova et al. measured biomass using absorbance at 600 nm, here culturable bacteria were determined by measuring CFU. It is normally observed that under stress conditions viable and culturable microorganisms differ due to the appearance of viable but not culturable bacteria [67]. Our calculations indicated that 1.0·10⁻⁴ M Zn²⁺, the same concentration obtained after 20 h for C(++) coatings, yielded a 92.2% *S. aureus* CFU inhibition. These results explained the antibacterial properties of ZnO coatings in the dark experiments. The additional inhibition observed under irradiation was the consequence of photogenerated ROS.

To check the ROS hypothesis, the presence of ROS in the liquid supernatant culture was measured by DCF fluorescence intensity. The results are presented in Fig. S4 (SM) and showed that ZnO-functionalized and irradiated surfaces were associated to an overproduction of intracellular ROS with a 7–15 % increase in the intensity of the DCF signal. The fact that specimens kept in the dark also overexpressed ROS with respect to non-functionalized surfaces can be explained by two mechanisms: (i) bioavailable dissolved zinc entering cells increases intracellular ROS and produces toxic damage [60], and (ii) electrons provided by ZnO surface defects reduce oxygen to form superoxide radicals [62,68].

Live/Dead, FilmTracer SYPRO Ruby Biofilm Matrix Stain and SEM images of *S. aureus* on uncoated and coated surfaces are shown in Figs. 6 and S5 (SM). In both aerosol and liquid contact modes the presence of photocatalytic material on the surface drastically decreases the number of viable bacteria as revealed by the Live/Dead staining. In the deposition of microorganisms-containing aerosol, upon Winter irradiation, L(+), most cells became red-marked and therefore it indicates membrane-damaged and non-viable bacteria. The explanation is that irradiation induced ROS production that caused membrane cell damage. Bacteria on non-functionalized surfaces appeared yellowish, which are considered viable, but probably endangered by the stress produced by a reduced nutrient availability in the droplets deposited on the surface of the tested specimens. In the liquid exposure mode, the surface images of the specimens revealed a high amount of viable, green-stained cells in controls, which decreased in the ZnO-functionalized surfaces. Biofilm formation was visualized by means of FilmTracer SYPRO Ruby Stain, which labels the constituent proteins of the extracellular polymeric substances (EPS) excreted by many microorganisms. EPS are normally attached to the cell and provide them with a protective structure, promoting the initial colonization of surfaces by planktonic microorganisms [69,70]. The results showed that biofilm formation was clearly inhibited in ZnO coated surfaces and this effect was amplified under irradiation. C(+L+) specimens presented a clear reduction of the biofilm adhered to the surface (Fig. 6) and C(+L++) coatings appeared essentially free of biofilm matrix in both aerosol and liquid contact modes (Fig. S5). SEM micrographs showed extensive bacterial colonization of non-functionalized specimens and a relatively small number of cells attached to the ZnO coated surfaces. SEM images also show size decrease and bacterial shape alteration in *S. aureus* cells in contact with ZnO, compatible with a loss of membrane integrity.

The results of this study showed that the differences in the antimicrobial performance between lower, C(+), and higher, C(++), ZnO mass surface density were not significant ($p > 0.5$ for growth inhibition). This observation is consistent with the fact that ZnO solubility limited the amount of zinc ions released up to a similar level for both coatings. Furthermore, the photogeneration of ROS occurs on the photocatalyst surface, which was almost equivalent (Fig. S4) as in

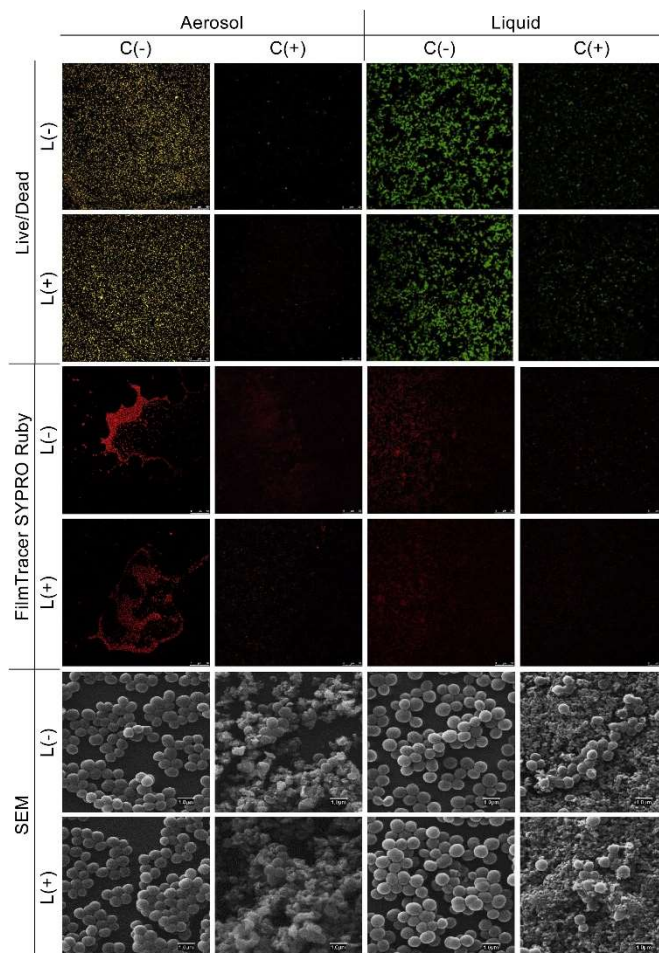


Figure 6. Live/Dead, FilmTracer SYPRO Ruby Biofilm Matrix Stain and SEM images of *S. aureus* on uncoated, C(-), and low loading, C(+), ZnO-functionalized surfaces in absence of irradiation, L(-), and upon L(+) irradiation, both in aerosol and liquid contact modes.

both cases ZnO particles completely covered the surface of the glass coverslips. The slight increase observed in ROS photogeneration at higher thickness could be explained by a more homogeneous coating with C(++) specimens. Contrarily, a significant increase in the bactericidal effect was found between Winter-Fall and Summer-Spring irradiation conditions. The fact that Zn^{2+} release and ROS intracellular overproduction take place even in the dark, indicates that UV irradiation is not the sole factor behind the antimicrobial activity of these ZnO coatings. This fact is more evident in those experiments carried out

with liquid contact. However, using the aerosol contact mode where dissolution of zinc ions is minimized, the antimicrobial action triggered by light is clear. Photogenerated ROS contribute to ZnO toxicity but the difference between dark and irradiated conditions is not as high as generally observed for other photocatalysts like TiO₂. Accordingly, Adams et al. reported that UV irradiation had lower influence on ZnO antibacterial properties compared with TiO₂ [51]. ZnO coatings, on the other hand, keep excellent performance during dark periods, including night or low irradiation scenarios.

4. Conclusions

The explored sol-gel approach was suitable to produce adequate ZnO suspensions for creating electrosprayed coatings. The size of particle aggregates deposited on functionalized surfaces were in the 100–300 nm range for surface densities not higher than 0.30 mg cm⁻². A good correlation was observed between aggregates dimension and droplet size calculated from scaling laws.

The ZnO electrosprayed surface corresponded to wurtzite structure with 33 nm crystal size. Functionalized surfaces exhibited photo-induced hydrophilicity under UV irradiation, increasing its wettability to water contact angles < 10° upon simulated either Winter or Summer irradiation.

The fabricated coatings showed excellent photocatalytic self-cleaning properties with > 95% MB degradation after 120 min irradiation. The combined antibacterial activity of electrosprayed surfaces led to > 99.5% (2-log) reduction in the number of culturable cells when exposed to sprayed bacterial cultures. In contact with liquid cultures and for cells detached from coating surface, > 99.9% inhibition (3-log reduction) was reached.

In both aerosol and liquid contact modes the presence of photocatalytic material on the surface greatly inhibits the formation of biofilm matrix on functionalized materials. The extracellular network of polymeric substances forming biofilm structure was absent from ZnO-electrosprayed surfaces as revealed by FilmTracer SYPRO Ruby staining.

The antimicrobial effect was attributed to a combination photogenerated ROS and bioavailable Zn²⁺ ions produced from ZnO dissolution to its solubility limit, which was approximately 10⁻⁴ M. Bacterial impairment took place through membrane damage and oxidative stress upon contact with the external coating surface. ZnO coatings kept antimicrobial performance during dark periods, which explains the relatively low difference found between low and high irradiation scenarios.

Acknowledgements

Financial support for this work was provided by Fundación Ramón Areces through the project OTR02666. LV thanks the Spanish Ministry of Education for the FPU grant FPU17/03096. The authors thank ICTS “NANBIOSIS” for the use of Confocal Microscopy Service.

References

- [1] M. Salwiczek, Y. Qu, J. Gardiner, R.A. Strugnell, T. Lithgow, K.M. McLean, H. Thissen, Emerging rules for effective antimicrobial coatings, *Trends Biotechnol.*, 32 (2014) 82-90.
- [2] B. Wang, Z. Ye, Q. Xu, H. Liu, Q. Lin, H. Chen, K. Nan, Construction of a temperature-responsive terpolymer coating with recyclable bactericidal and self-cleaning antimicrobial properties, *Biomater. Sci.*, 4 (2016) 1731-1741.
- [3] I.A. Tudor, M. Petriceanu, R.R. Piticescu, R.M. Piticescu, C. Predescu, Hydrothermal synthesis of doped ZnO and TiO₂ nanomaterials: Opportunities for textile applications, *UPB Scientific Bulletin, Series B: Chemistry and Materials Science*, 76 (2014) 207-215.
- [4] A. Behzadnia, M. Montazer, M.M. Rad, In-situ sonosynthesis of nano N-doped ZnO on wool producing fabric with photo and bio activities, cell viability and enhanced mechanical properties, *J. Photochem. Photobiol., B*, 149 (2015) 103-115.
- [5] V.K. Yemmireddy, Y.-C. Hung, Using photocatalyst metal oxides as antimicrobial surface coatings to ensure food safety—Opportunities and challenges, *Compr. Rev. Food Sci. Food Saf.*, 16 (2017) 617-631.
- [6] F. Lu, W. Cai, Y. Zhang, ZnO hierarchical micro/nanoarchitectures: Solvothermal synthesis and structurally enhanced photocatalytic performance, *Adv. Funct. Mater.*, 18 (2008) 1047-1056.
- [7] J.S. Na, B. Gong, G. Scarel, G.N. Parsons, Surface polarity shielding and hierarchical ZnO nano-architectures produced using sequential hydrothermal crystal synthesis and thin film atomic layer deposition, *ACS Nano*, 3 (2009) 3191-3199.
- [8] A. Janotti, C.G. Van de Walle, Fundamentals of zinc oxide as a semiconductor, *Rep. Prog. Phys.*, 72 (2009) 126501.
- [9] L. Anat, N. Yeshayahu, G. Aharon, L. Rachel, Antifungal activity of ZnO nanoparticles—the role of ROS mediated cell injury, *Nanotechnology*, 22 (2011) 105101.
- [10] R. Jalal, E.K. Goharshadi, M. Abareshi, M. Moosavi, A. Yousefi, P. Nancarrow, ZnO nanofluids: Green synthesis, characterization, and antibacterial activity, *Mater. Chem. Phys.*, 121 (2010) 198-201.
- [11] K.R. Raghupathi, R.T. Koodali, A.C. Manna, Size-Dependent Bacterial Growth Inhibition and Mechanism of Antibacterial Activity of Zinc Oxide Nanoparticles, *Langmuir*, 27 (2011) 4020-4028.
- [12] J. Sawai, S. Shoji, H. Igarashi, A. Hashimoto, T. Kokugan, M. Shimizu, H. Kojima, Hydrogen peroxide as an antibacterial factor in zinc oxide powder slurry, *J. Ferment. Bioeng.*, 86 (1998) 521-522.

- [13] L. Zhang, Y. Ding, M. Povey, D. York, ZnO nanofluids – A potential antibacterial agent, *Prog. Nat. Sci.*, 18 (2008) 939-944.
- [14] X. Bellanger, P. Billard, R. Schneider, L. Balan, C. Merlin, Stability and toxicity of ZnO quantum dots: Interplay between nanoparticles and bacteria, *J. Hazard. Mater.*, 283 (2015) 110-116.
- [15] T.J. Brunner, P. Wick, P. Manser, P. Spohn, R.N. Grass, L.K. Limbach, A. Bruinink, W.J. Stark, In vitro cytotoxicity of oxide nanoparticles: Comparison to asbestos, silica, and the effect of particle solubility, *Environ. Sci. Technol.*, 40 (2006) 4374-4381.
- [16] K. Kasemets, A. Ivask, H.-C. Dubourguier, A. Kahru, Toxicity of nanoparticles of ZnO, CuO and TiO₂ to yeast *Saccharomyces cerevisiae*, *Toxicol. in Vitro*, 23 (2009) 1116-1122.
- [17] M. Li, L. Zhu, D. Lin, Toxicity of ZnO nanoparticles to *Escherichia coli*: Mechanism and the influence of medium components, *Environ. Sci. Technol.*, 45 (2011) 1977-1983.
- [18] R. Brayner, R. Ferrari-Iliou, N. Brivois, S. Djediat, M.F. Benedetti, F. Fiévet, Toxicological impact studies based on *Escherichia coli* bacteria in ultrafine ZnO nanoparticles colloidal medium, *Nano Lett.*, 6 (2006) 866-870.
- [19] L. Zhang, Y. Jiang, Y. Ding, M. Povey, D. York, Investigation into the antibacterial behaviour of suspensions of ZnO nanoparticles (ZnO nanofluids), *J. Nanopart. Res.*, 9 (2007) 479-489.
- [20] Y. Liu, L. He, A. Mustapha, H. Li, Z.Q. Hu, M. Lin, Antibacterial activities of zinc oxide nanoparticles against *Escherichia coli* O157:H7, *Journal of Applied Microbiology*, 107 (2009) 1193-1201.
- [21] N. Jones, B. Ray, K.T. Ranjit, A.C. Manna, Antibacterial activity of ZnO nanoparticle suspensions on a broad spectrum of microorganisms, *FEMS Microbiol. Lett.*, 279 (2008) 71-76.
- [22] S. Kavadiya, D.M. Niedzwiedzki, S. Huang, P. Biswas, Electro spray-assisted fabrication of moisture-resistant and highly stable perovskite solar cells at ambient conditions, *Adv. Energy Mater.*, 7 (2017) 1700210.
- [23] A. Jaworek, Electro spray droplet sources for thin film deposition, *J. Mater. Sci.*, 42 (2007) 266-297.
- [24] A. Jaworek, A.T. Sobczyk, Electro spraying route to nanotechnology: An overview, *J. Electrostat.*, 66 (2008) 197-219.
- [25] X. Li, P. Guerieri, W. Zhou, C. Huang, M.R. Zachariah, Direct deposit laminate nanocomposites with enhanced propellant properties, *ACS Appl. Mater. Interfaces*, 7 (2015) 9103-9109.
- [26] Y. He, Y. Huang, W. Wang, Y. Cheng, Integrating micromixer precipitation and electro spray drying toward continuous production of drug nanoparticles, *Chem. Eng. J.*, 168 (2011) 931-937.
- [27] L. Spanhel, M.A. Anderson, Semiconductor clusters in the sol-gel process: quantized aggregation, gelation, and crystal growth in concentrated zinc oxide colloids, *J. Am. Chem. Soc.*, 113 (1991) 2826-2833.
- [28] Y. Hara, J. Brownson, M. Anderson, Solvothermal fabrication of ZnO nanorods using ethanolic quantum dot precursors, *Physica Status Solidi (a)*, 206 (2009) 711-717.
- [29] P.K. Mishra, H. Mishra, A. Ekielski, S. Talegaonkar, B. Vaidya, Zinc oxide nanoparticles: a promising nanomaterial for biomedical applications, *Drug Discovery Today*, 22 (2017) 1825-1834.
- [30] A. Daerr, A. Mogne, Pendent_Drop: An ImageJ plugin to measure the surface tension from an image of a pendent drop, *J. Open Res. Software*, 4 (2016) p.e3.
- [31] R. Atchudan, T.N.J.I. Edison, S. Perumal, D. Karthikeyan, Y.R. Lee, Facile synthesis of zinc oxide nanoparticles decorated graphene oxide composite via simple solvothermal route and their photocatalytic activity on methylene blue degradation, *J. Photochem. Photobiol., B*, 162 (2016) 500-510.
- [32] W. Shen, Z. Li, H. Wang, Y. Liu, Q. Guo, Y. Zhang, Photocatalytic degradation for methylene blue using zinc oxide prepared by codeposition and sol-gel methods, *J. Hazard. Mater.*, 152 (2008) 172-175.
- [33] OIML, The scale of relative humidity of air certified against saturated salt solutions, in: *International recommendation, OIML, Organisation Internationale de Métrologie Légale, Paris, 1996.*
- [34] A. Gomes, E. Fernandes, J.L.F.C. Lima, Fluorescence probes used for detection of reactive oxygen species, *J. Biochem. Biophys. Methods*, 65 (2005) 45-80.
- [35] B. Kalyanaraman, V. Darley-Usmar, K.J.A. Davies, P.A. Dennery, H.J. Forman, M.B. Grisham, G.E. Mann, K. Moore, L.J. Roberts, H. Ischiropoulos, Measuring reactive oxygen and nitrogen species with fluorescent probes: Challenges and limitations, *Free Radical Biology and Medicine*, 52 (2012) 1-6.
- [36] S. Goutelle, M. Maurin, F. Rougier, X. Barbaut, L. Bourguignon, M. Ducher, P. Maire, The Hill equation: a review of its capabilities in pharmacological modelling, *Fundamental & Clinical Pharmacology*, 22 (2008) 633-648.
- [37] A. Król, P. Pomastowski, K. Rafińska, V. Railean-Plugaru, B. Buszewski, Zinc oxide nanoparticles: Synthesis, antiseptic activity and toxicity mechanism, *Adv. Colloid Interface Sci.*, 249 (2017) 37-52.
- [38] A. Sirelkhatim, S. Mahmud, A. Seeni, N.H.M. Kaus, L.C. Ann, S.K.M. Bakhori, H. Hasan, D. Mohamad, Review on zinc oxide nanoparticles: Antibacterial activity and toxicity mechanism, *Nano-Micro Letters*, 7 (2015) 219-242.
- [39] E. Castillo-Orozco, A. Kar, R. Kumar, Electro spray mode transition of microdroplets with semiconductor nanoparticle suspension, *Sci. Rep.*, 7 (2017) 5144.
- [40] B. Vonnegut, R.L. Neubauer, Production of monodisperse liquid particles by electrical atomization, *Journal of Colloid Science*, 7 (1952) 616-622.
- [41] J. Fernández de La Mora, I.G. Loscertales, The current emitted by highly conducting Taylor cones, *J. Fluid Mech.*, 260 (1994) 155-184.
- [42] A.M. Gañan-Calvo, 20.0.05 The size and charge of droplets in the electro spraying of polar liquids in cone-jet mode, and the minimum droplet size, *J. Aerosol Sci.*, 25 (1994) 309-310.
- [43] D.-R. Chen, D.Y.H. Pui, Experimental investigation of scaling laws for electro spraying: Dielectric constant effect, *Aerosol Sci. Technol.*, 27 (1997) 367-380.
- [44] V. Khranovskyy, T. Ekblad, R. Yakimova, L. Hultman, Surface morphology effects on the light-controlled

- wettability of ZnO nanostructures, *Appl. Surf. Sci.*, 258 (2012) 8146-8152.
- [45] M.T.Z. Myint, N.S. Kumar, G.L. Hornyak, J. Dutta, Hydrophobic/hydrophilic switching on zinc oxide micro-textured surface, *Appl. Surf. Sci.*, 264 (2013) 344-348.
- [46] A.P. Rambu, V. Tiron, V. Nica, N. Iftimie, Functional properties of ZnO films prepared by thermal oxidation of metallic films, *J. Appl. Phys.*, 113 (2013) 234506
- [47] E. Velayi, R. Norouzbeigi, Annealing temperature dependent reversible wettability switching of micro/nano structured ZnO superhydrophobic surfaces, *Appl. Surf. Sci.*, 441 (2018) 156-164.
- [48] S. Karuppuchamy, S. Ito, Cathodic electrodeposition of nanoporous ZnO thin films from new electrochemical bath and their photoinduced hydrophilic properties, *Vacuum*, 82 (2008) 547-550.
- [49] R.D. Sun, A. Nakajima, A. Fujishima, T. Watanabe, K. Hashimoto, Photoinduced surface wettability conversion of ZnO and TiO₂ thin films, *J. Phys. Chem. B*, 105 (2001) 1984-1990.
- [50] Y.J. Jang, C. Simer, T. Ohm, Comparison of zinc oxide nanoparticles and its nano-crystalline particles on the photocatalytic degradation of methylene blue, *Mater. Res. Bull.*, 41 (2006) 67-77.
- [51] L.K. Adams, D.Y. Lyon, P.J.J. Alvarez, Comparative eco-toxicity of nanoscale TiO₂, SiO₂, and ZnO water suspensions, *Water Res.*, 40 (2006) 3527-3532.
- [52] Z. Huang, X. Zheng, D. Yan, G. Yin, X. Liao, Y. Kang, Y. Yao, D. Huang, B. Hao, Toxicological effect of ZnO nanoparticles based on bacteria, *Langmuir*, 24 (2008) 4140-4144.
- [53] T. Xia, M. Kovoichich, M. Liong, L. Mädler, B. Gilbert, H. Shi, J.I. Yeh, J.I. Zink, A.E. Nel, Comparison of the mechanism of toxicity of zinc oxide and cerium oxide nanoparticles based on dissolution and oxidative stress properties, *ACS Nano*, 2 (2008) 2121-2134.
- [54] T.S. Justin, J.W. Thomas, Antibacterial effect of zinc oxide nanoparticles combined with ultrasound, *Nanotechnology*, 23 (2012) 495101.
- [55] K. Kairyte, A. Kadys, Z. Luksiene, Antibacterial and antifungal activity of photoactivated ZnO nanoparticles in suspension, *J. Photochem. Photobiol., B*, 128 (2013) 78-84.
- [56] L. Zhang, Y. Jiang, Y. Ding, N. Daskalakis, L. Jeuken, M. Povey, A.J. O'Neill, D.W. York, Mechanistic investigation into antibacterial behaviour of suspensions of ZnO nanoparticles against *E. coli*, *J. Nanopart. Res.*, 12 (2010) 1625-1636.
- [57] E.A.S. Dimapilis, C.-S. Hsu, R.M.O. Mendoza, M.-C. Lu, Zinc oxide nanoparticles for water disinfection, *Sustainable Environ. Res.*, 28 (2018) 47-56.
- [58] L.S. Reddy, M.M. Nisha, M. Joice, P.N. Shilpa, Antimicrobial activity of zinc oxide (ZnO) nanoparticle against *Klebsiella pneumoniae*, *Pharm. Biol.*, 52 (2014) 1388-1397.
- [59] M. Premanathan, K. Karthikeyan, K. Jeyasubramanian, G. Manivannan, Selective toxicity of ZnO nanoparticles toward Gram-positive bacteria and cancer cells by apoptosis through lipid peroxidation, *Nanomedicine: Nanotechnology, Biology and Medicine*, 7 (2011) 184-192.
- [60] W. Song, J. Zhang, J. Guo, J. Zhang, F. Ding, L. Li, Z. Sun, Role of the dissolved zinc ion and reactive oxygen species in cytotoxicity of ZnO nanoparticles, *Toxicol. Lett.*, 199 (2010) 389-397.
- [61] B.A. Holt, S.A. Gregory, T. Sulchek, S. Yee, M.D. Losego, Aqueous zinc compounds as residual antimicrobial agents for textiles, *ACS Appl. Mater. Interfaces*, 10 (2018) 7709-7716.
- [62] R. Kumar, A. Umar, G. Kumar, H.S. Nalwa, Antimicrobial properties of ZnO nanomaterials: A review, *Ceram. Int.*, 43 (2017) 3940-3961.
- [63] J. Pasquet, Y. Chevalier, J. Pelletier, E. Couval, D. Bouvier, M.-A. Bolzinger, The contribution of zinc ions to the antimicrobial activity of zinc oxide, *Colloids and Surfaces A: Physicochemical and Engineering Aspects*, 457 (2014) 263-274.
- [64] B. Wu, Y. Wang, Y.-H. Lee, A. Horst, Z. Wang, D.-R. Chen, R. Sureshkumar, Y.J. Tang, Comparative ecotoxicities of nano-ZnO particles under aquatic and aerosol exposure modes, *Environ. Sci. Technol.*, 44 (2010) 1484-1489.
- [65] C.A. David, J. Galceran, C. Rey-Castro, J. Puy, E. Companys, J. Salvador, J. Monné, R. Wallace, A. Vakourov, Dissolution kinetics and solubility of ZnO nanoparticles followed by AGNES, *J. Phys. Chem. C*, 116 (2012) 11758-11767.
- [66] D. Chudobova, S. Dostalova, B. Ruttkay-Nedecky, R. Guran, M.A.M. Rodrigo, K. Tmejova, S. Krizkova, O. Zitka, V. Adam, R. Kizek, The effect of metal ions on *Staphylococcus aureus* revealed by biochemical and mass spectrometric analyses, *Microbiol. Res.*, 170 (2015) 147-156.
- [67] D. Venieri, E. Chatzisyneon, M.S. Gonzalo, R. Rosal, D. Mantzavinos, Inactivation of *Enterococcus faecalis* by TiO₂-mediated UV and solar irradiation in water and wastewater: culture techniques never say the whole truth, *Photochem. Photobiol. Sci.*, 10 (2011) 1744-1750.
- [68] V. Lakshmi Prasanna, R. Vijayaraghavan, Insight into the mechanism of antibacterial activity of ZnO: Surface defects mediated reactive oxygen species even in the dark, *Langmuir*, 31 (2015) 9155-9162.
- [69] B. Jalvo, M. Faraldos, A. Bahamonde, R. Rosal, Antimicrobial and antibiofilm efficacy of self-cleaning surfaces functionalized by TiO₂ photocatalytic nanoparticles against *Staphylococcus aureus* and *Pseudomonas putida*, *J. Hazard. Mater.*, 340 (2017) 160-170.
- [70] H. Liu, H.H.P. Fang, Extraction of extracellular polymeric substances (EPS) of sludges, *J. Biotechnol.*, 95 (2002) 249-256.

Supplementary Material

Antimicrobial surfaces with self-cleaning properties functionalized by photocatalytic ZnO electro sprayed coatings

Laura Valenzuela^{1,2}, Ana Iglesias^{2,*}, Marisol Faraldos^{2,*}, Ana Bahamonde², Roberto Rosal^{1,*}

¹ Department of Chemical Engineering, University of Alcalá, E-28871 Alcalá de Henares, Madrid, Spain

² Instituto de Catálisis y Petroleoquímica, ICP-CSIC, Marie Curie 2, 28049 Madrid, Spain

Corresponding authors: ana.iglesias@icp.csic.es, mfaraldos@icp.csic.es, roberto.rosal@uah.es

Contents:

Figure S1. Schematic representation of the sealed aerosol deposition chamber for photocatalytic bioassays: (1) Microorganisms-containing aerosol, (2) ZnO coated and uncoated glass coverslips, (3) hygrostatic K₂SO₄ solution.

Table S1. Properties of ZnO nanoparticle suspension and scaling laws for the operated electro spray system.

Figure S2. Solubility of zinc ion (Zn²⁺) from electro sprayed ZnO coatings in Milli-Q water at 37°C over time.

Figure S3. Dose-response curve of zinc ion (Zn²⁺) to *S. aureus* and sigmoidal Hill equation fitting.

Figure S4. Relative fluorescence units (RFU) of intracellular DCF due to ROS production in the supernatant for the liquid in contact with uncoated, C(-), low loading, C(++), and high loading, C(++), ZnO coatings. Experiments in the absence of irradiation (■), and upon L(+) (■) and L(++)(■) irradiation.

Figure S5. Live/Dead, FilmTracer SYPRO Ruby Biofilm Matrix Stain and SEM images of *S. aureus* on uncoated, C(-), low loading, C(+), and high loading, C(++), ZnO coatings in the absence of irradiation, L(-), and upon L(+) and L(++)(■) irradiation both in aerosol and liquid bacterial exposure modes.

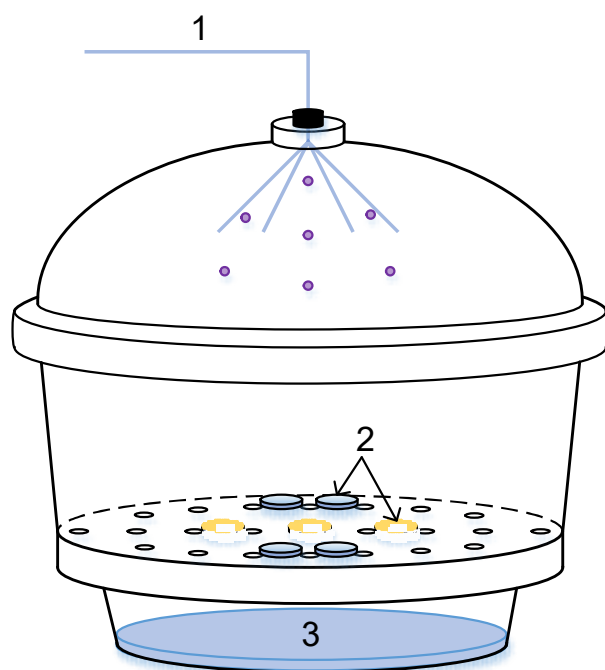


Figure S1. Schematic representation of the sealed aerosol deposition chamber for photocatalytic bioassays: (1) Microorganisms-containing aerosol, (2) ZnO coated and uncoated glass coverslips, (3) hygrostatic K_2SO_4 solution.

Table S1. Properties of ZnO nanoparticle suspension and scaling laws for the operated electrospray system.

Properties of ZnO nanoparticle suspension	
Surface tension (γ)	0.03341 N m ⁻¹
Solvent density (ρ)	792 kg m ⁻³
Electrical conductivity (K)	0.664 S m ⁻¹
Solvent dielectric constant (κ)	32.6
Feed flow rate (Q)	1.39 · 10 ⁻¹¹ m ³ s ⁻¹
Vacuum permittivity (ϵ_0)	8.85 · 10 ⁻¹² C ² N ⁻¹ m ⁻²
Charge relaxation time (τ , $\kappa\epsilon_0/K$)	4.35 · 10 ⁻¹⁰ s
Scaling laws	
Fernández de la Mora (1994)	Gañán-Calvo (1994)
Droplet size (D_d)	
$G(\kappa) = 10.87\kappa^{-6/5} + 4.08\kappa^{-1/3}$ $G(\kappa) = 1.44$ $D_d = G(\kappa)(Q\tau)^{1/3}$ $D_d = 263 \text{ nm}$	$k_d = 1.66$ $D_d = k_d\kappa^{-1/6}(Q\tau)^{1/3}$ $D_d = 540 \text{ nm}$
Current emitted (I)	
$f(\kappa) = -449 - 0.21\kappa + 157\kappa^{1/6} + 336\kappa^{-1/6}$ $f(\kappa) = 12.75$ $I = f(\kappa) \left(\frac{\gamma K Q}{\kappa} \right)^{1/2}$ $I = 0.001 \text{ mA}$	$k_I = 6.46$ $I = k_I\kappa^{1/4} \left(\frac{\gamma K Q}{\kappa} \right)^{1/2}$ $I = 0.002 \text{ mA}$
Minimum feeding flow rate (Q_{min})	
$Q_{min} = \frac{\kappa\epsilon_0\gamma}{\rho K}$ $Q_{min} = 1.83 \cdot 10^{-14} \text{ m}^3 \text{ s}^{-1}$	$Q_{min} = \frac{\kappa^{1/2}\epsilon_0\gamma}{\rho K}$ $Q_{min} = 3.21 \cdot 10^{-15} \text{ m}^3 \text{ s}^{-1}$

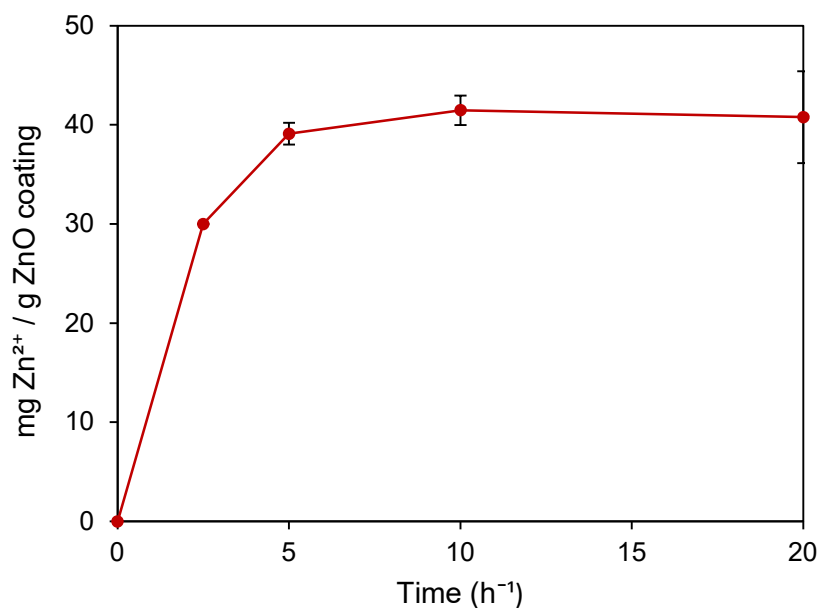


Figure S2. Solubility of zinc ion (Zn^{2+}) from electrospayed ZnO coatings in Milli-Q water at 37°C over time.

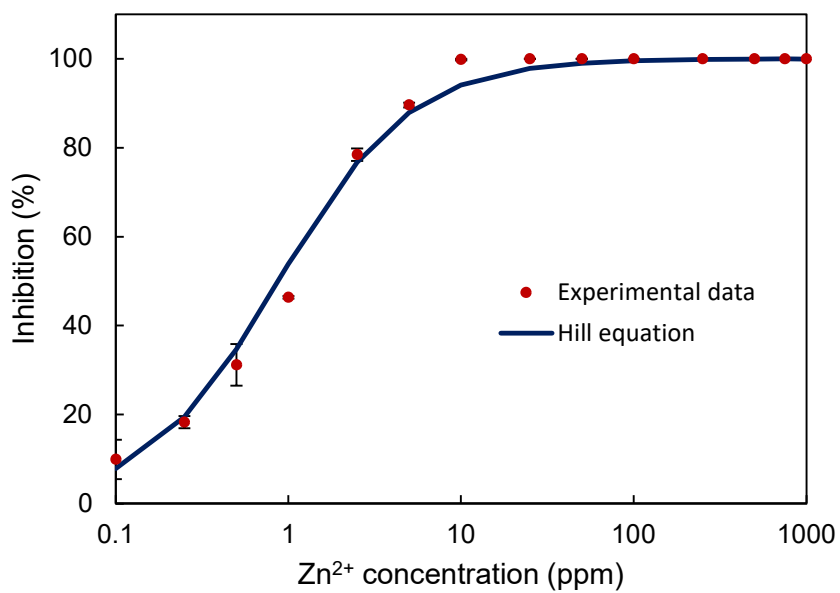


Figure S3. Dose-response curve of zinc ion (Zn^{2+}) to *S. aureus* and sigmoidal Hill equation fitting.

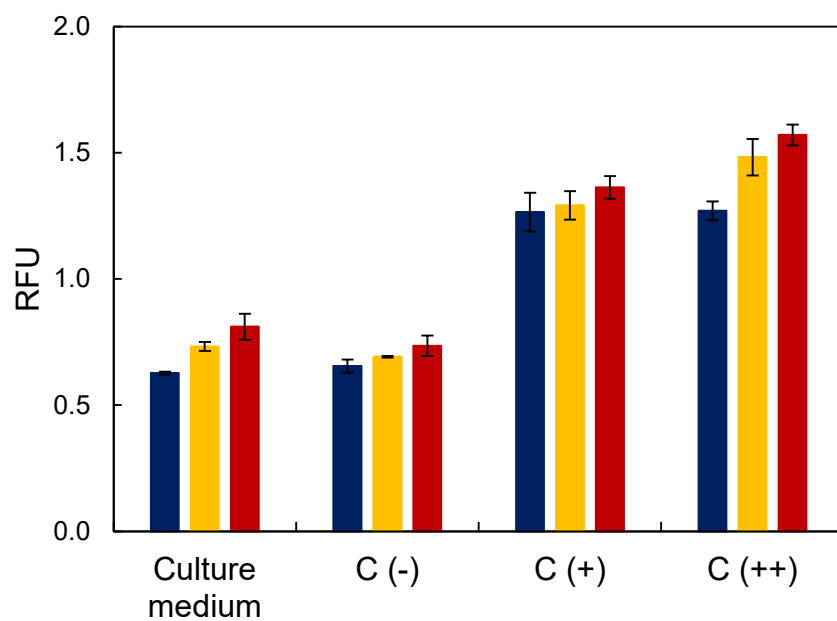


Figure S4. Relative fluorescence units (RFU) of intracellular DCF due to ROS production in the supernatant for the liquid in contact with uncoated, C(-), low loading, C(++), and high loading, C(++), ZnO coatings. Experiments in the absence of irradiation (■), and upon L(+) (■) and L(++) (■) irradiation.

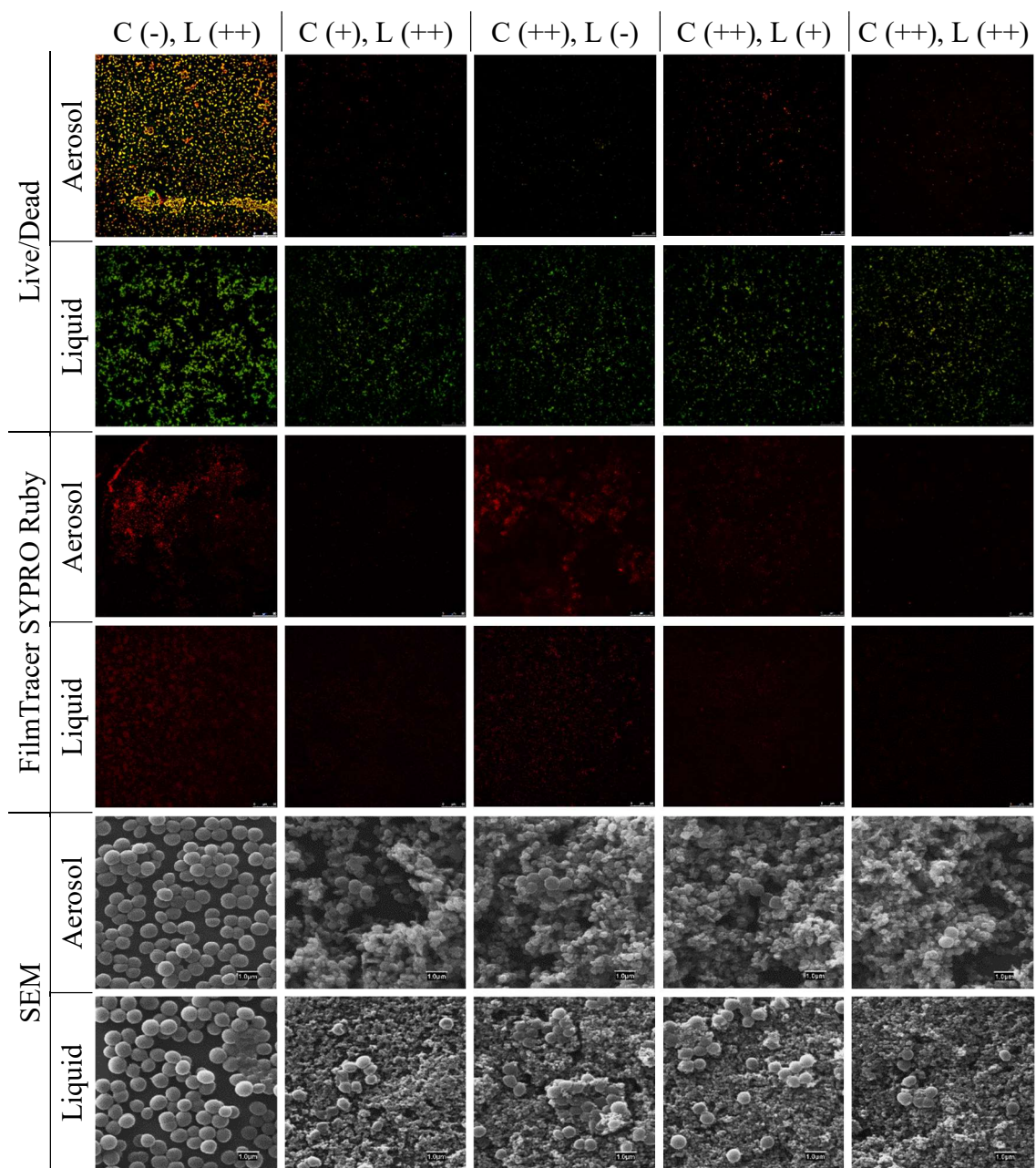


Figure S5. Live/Dead, FilmTracer SYPRO Ruby Biofilm Matrix Stain and SEM images of *S. aureus* on uncoated, C(-), low loading, C(+), and high loading, C(++), ZnO coatings in the absence of irradiation, L(-), and upon L(+) and L(++) irradiation both in aerosol and liquid contact modes.